

# On the crystalline environment of luminescent $\text{Tb}^{3+}$ ions embedded in indium tin oxide thin films: a DFT and Crystal field analysis assessment

E. Serquen<sup>1,\*</sup>, K. Lizárraga<sup>1,2</sup>, L. A. Enrique<sup>1</sup>, F. Bravo<sup>1</sup>, S. Mishra<sup>1</sup>,

P. LLontop<sup>3</sup>, P. Venezuela<sup>2</sup>, L. R. Tessler<sup>4</sup>, and J. A. Guerra<sup>1†</sup>

<sup>1</sup>Departamento de Ciencias, Sección Física, Pontificia Universidad Católica del Perú, Av. Universitaria 1801, 15088, Lima, Perú

<sup>2</sup>Instituto de Física, Universidade Federal Fluminense, 24210-346, Niterói, RJ, Brazil

<sup>3</sup>MESA+ Institute for Nanotechnology, University of Twente, Enschede 7500 AE, The Netherlands. and

<sup>4</sup>Instituto de Física Gleb Wataghin, Universidade Estadual de Campinas, 13083-859, Campinas, SP, Brazil

(Dated: February 13, 2025)

We assess the local symmetry and crystal environment of trivalent terbium ions embedded in an indium tin oxide (ITO) matrix with bixbyite structure. The  $\text{Tb}^{3+}$  ions tend to substitute  $\text{In}^{3+}$  ions in two different cationic sites (*b* and *d*). Density Functional Theory (DFT) calculations suggest that the  $\text{Tb}^{3+}$  ions are mainly located at  $C_2$  symmetry sites relaxing selection rules and enabling electric dipole transitions, with the  $^5\text{D}_4 \rightarrow ^7\text{F}_2$  transition being the most intense, providing a red color to the light emission. Photoluminescence emission spectra under UV excitation at 83 K revealed 30 intra-4f transitions, which were assigned to the  $^7\text{F}_J$  ground multiplet of the  $\text{Tb}^{3+}$  ion. Crystal-field analysis shows a strong alignment between calculated and observed energy levels, yielding a standard deviation of  $\sigma = 15.1 \text{ cm}^{-1}$ . We believe these results can help to understand the activation mechanisms of  $\text{Tb}^{3+}$  luminescent centers in transparent conductive oxides, as well as the potential to modulate  $\text{Tb}^{3+}$  emission color through its crystalline environment.

## I. INTRODUCTION

Trivalent rare earth (RE) ions have the capability to emit light when incorporated in some transparent host materials covering a wide range of the visible spectrum. Their distinctive spectroscopic properties primarily arise from electronic transitions within their partially filled  $4f^n$  orbitals ( $n=0-14$ ). Intra-4f electric dipole (ED) transitions are forbidden by Laporte selection rules and only magnetic dipole (MD) transitions are allowed in the free ion case. However, when RE ions are embedded into a matrix occupying a non-centrosymmetric site in the host lattice, the interactions with the crystal field (CF) mix electronic states having opposite parity. The free ion 4f energy levels split under the influence of the local electric field produced by the crystalline environment, with the point symmetry around the ion being the only factor that determines how much the degeneracy of the free-ion state is removed [1, 2].

Among RE ions, terbium ( $\text{Tb}^{3+}$ ) has been widely used as a dopant of wide and ultra-wide bandgap semiconductor host materials, such as SiC,  $\text{Ga}_2\text{O}_3$ , AlN, ZnO, a-SiN:H, and GaN [3–8]. The energy transfer from the host to the  $\text{Tb}^{3+}$  ions enables them to act as functional luminescent centers, with the  $^5\text{D}_4 \rightarrow ^7\text{F}_5$  transition in the green regions around 545 nm being typically the most intense. This makes  $\text{Tb}^{3+}$  ions ideal to be used as green phosphorus for photon downshift layers, as well as down- and up-conversion layers, biomarkers, fluorescent lamps, optical fiber temperature sensors, and LEDs [9–13]. Nevertheless, the emission color of the  $\text{Tb}^{3+}$  ions can be influenced by the chemical environment and the excitation

process. For instance, it has been previously reported the capability to tune the color emission of  $\text{Tb}^{3+}$  ions by reducing the Tb concentration in the host matrix, leading to an increase in the blue emission, related to  $^5\text{D}_3 \rightarrow ^7\text{F}_{4,5,6}$  transitions, while all other transitions intensities are quenched [14–16].

In the last decade, Transparent Conductive Oxides (TCOs) have emerged as promising host materials for RE ions since they combine high optical transmittance in the UV-Vis range and electrical conductivity, making them key components in many optoelectronic devices [17]. The current trend of incorporating RE ions into TCOs aims to add luminescent properties to these materials. Thus, different host of TCOs based on  $\text{In}_2\text{O}_3$ ,  $\text{SnO}_2$ ,  $\text{CdO}$ ,  $\text{Ga}_2\text{O}_3$ , and  $\text{ZnO}$  have been doped with several RE ions [18–22]. One of the most investigated TCOs host materials is indium tin oxide (ITO;  $\text{SnO}_2$  doped  $\text{In}_2\text{O}_3$ ) [22–24]. The impact of  $\text{Tb}^{3+}$  incorporation on the electrical, optical, and light emission properties of ITO thin films has been recently investigated [25]. The latter study reported an unusually intense red-light emission from the  $\text{Tb}^{3+}$  ions, associated to  $^5\text{D}_4 \rightarrow ^7\text{F}_2$  transition. This transition can be resolved into five peaks due to Stark splitting, highlighting the crystal field effect on the  $\text{Tb}^{3+}$  ion in a low symmetry site.

In this work, we present experimental results validated by a theoretical analysis based on density functional theory (DFT) calculations and crystal field (CF) analysis to identify the local symmetry of the lattice site occupied by the  $\text{Tb}^{3+}$  ions in the ITO lattice with a bixbyite structure. Low temperature photoluminescence under UV excitation presented a multiple peak structure. The individual peaks were associated to transitions within the  $^7\text{F}_{JM}$  energy levels corresponding to  $C_2$  symmetry sites. Results show the remarkable relation between the local symmetry and  $\text{Tb}^{3+}$  emission color. These results may

\* Contact author: esserquen@pucp.edu.pe

† Contact author: guerra.jorgea@pucp.edu.pe

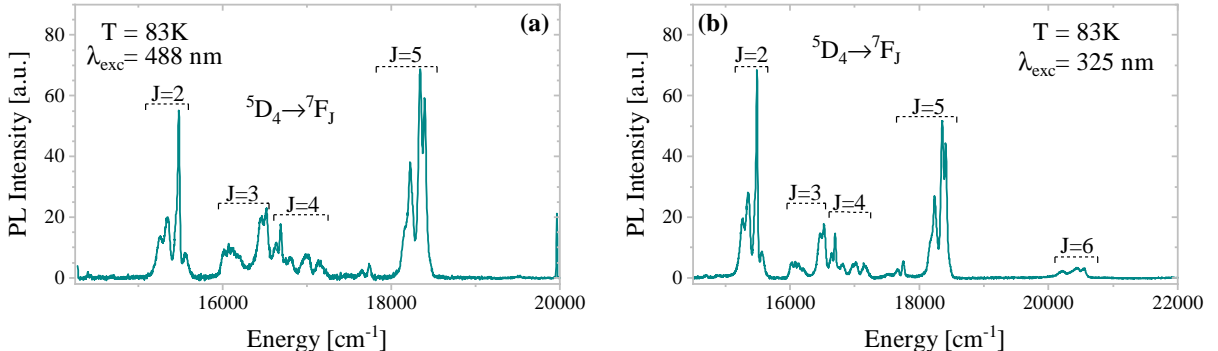


**FIG. 1:** Photoluminescence spectra at 83K under excitation wavelength of 488 nm (a), and 325 nm (b).  ${}^5\text{D}_4$  related electronic transitions are denoted.

be applied to host with similar symmetries allowing the tunability of the  $\text{Tb}^{3+}$  light emission color.

## II. EXPERIMENTAL DETAILS

The experimental procedures, including the synthesis method and characterization techniques can be found elsewhere [25]. For the sake of brevity, only a summary of the key aspects is provided here. ITO:Tb thin films were synthesized by magnetron sputtering technique using ITO (90 wt.%  $\text{In}_2\text{O}_3$  & 10 wt.%  $\text{SnO}_2$ ) and Tb targets. Photoluminescence activation was achieved after annealing at 650 °C in air.

Photoluminescence (PL) spectra were recorded in a Renishaw inVia micro-Raman spectrometer with HeCd (325 nm) and Ar (488 nm) laser excitation. Low temperature PL measurements were carried out in a Linkam THMS600 cooling stage with a liquid nitrogen inlet.

## III. RESULTS AND DISCUSSION

### A. $\text{Tb}^{3+}$ emission spectrum

PL spectra of the sample containing 1.5 at.% Tb at 83 K under 488 nm and 325 nm excitation are shown in Figure 1. The observed  $\text{Tb}^{3+}$  related emission corresponds to the  ${}^5\text{D}_4 \rightarrow {}^7\text{F}_J$  transitions. Figure 1(a) depicts the PL spectrum under sub-bandgap excitation with a 488 nm laser. This excitation is quasi-resonant with  ${}^5\text{D}_4 \rightarrow {}^7\text{F}_6$  transition. On the other hand, Figure 1(b) depicts the PL spectrum under a 325 nm wavelength excitation, which corresponds to sub-bandgap excitation involving band tail states ( $E_g = 3.82$  eV,  $E_U = 0.22$  eV) [25]. We did not observe any transitions associated with the  ${}^5\text{D}_3$  initial states. Since, the energy difference between the  ${}^5\text{D}_3$  and  ${}^5\text{D}_4$  level is approximately 5600 cm<sup>-1</sup> [26], and the phonon threshold in  $\text{In}_2\text{O}_3$  is around 300 cm<sup>-1</sup> [27], excited ions at  ${}^5\text{D}_3$  state could decay to the  ${}^5\text{D}_4$  state mediated by multiphonon relaxation.

However, at these Tb concentrations, a cross-relaxation process may also take place by the interaction between two neighboring  $\text{Tb}^{3+}$  ions, leading to the quenching of  ${}^5\text{D}_3$  related light emission as a result of the energy transfer from  ${}^5\text{D}_3 \rightarrow {}^5\text{D}_4$  to  ${}^7\text{F}_J$  manifold [15, 16].

To determine the fractional contribution of a specified measurable transition ( ${}^5\text{D}_J \rightarrow {}^7\text{F}_{J'}$ ) to the total radiative transition probability from the excited state, the relative intensities for each transition ( $\beta_{JJ'}$ ) were calculated according to:

$$\beta_{JJ'} = \frac{I_{JJ'}}{\sum I_{JJ'}} \quad (1)$$

Here  $I_{JJ'}$  is the integrated emission intensity of a specific  $J \rightarrow J'$  transition. The selection rules on the total angular quantum number  $J$  can help to identify the transition mechanism, i.e. electric dipole (ED) or magnetic dipole (MD) mediated. The  $J = 0 \rightarrow J' = 0$  transition is forbidden by ED and MD. MD transitions are subjected to the selection rules  $\Delta S = 0$ ,  $\Delta L = 0$ ,  $\Delta J = 0, \pm 1$ . Whereas, for ED transitions the selection rules  $\Delta S = 0$ ,  $\Delta L \leq 6$ , and  $\Delta J \leq 6$  apply, which can be further restricted to  $\Delta J = 2, 4, 6$  when either  $J = 0$  or  $J' = 0$  [28]. Table I summarizes the  $\beta_{JJ'}$  calculated from the spectrum measured under UV excitation, and the related transition mechanism.

**TABLE I:** Fractional contribution  $\beta_{JJ'}$  calculated from the spectrum under 325 nm excitation wavelength.

Transition	$\beta_{JJ'} [\%]$	Type
${}^5\text{D}_4 \rightarrow {}^7\text{F}_6$	2.95	ED
${}^5\text{D}_4 \rightarrow {}^7\text{F}_5$	28.53	ED + MD
${}^5\text{D}_4 \rightarrow {}^7\text{F}_4$	10.67	ED + MD
${}^5\text{D}_4 \rightarrow {}^7\text{F}_3$	15.03	ED + MD
${}^5\text{D}_4 \rightarrow {}^7\text{F}_2$	42.82	ED

Based on the selection rules, the  ${}^5\text{D}_4 \rightarrow {}^7\text{F}_5$  transition has a ED+MD mixed contribution, being typically the most prominent emission line. Notwithstanding, here the  ${}^5\text{D}_4 \rightarrow {}^7\text{F}_2$  ED transition exhibits the highest intensity

in our PL spectra. Such behavior might be caused by the high sensitivity of this transition to the inhomogeneities in the dielectric surrounding of the  $\text{Tb}^{3+}$  ions. This phenomenon has been previously predicted by Richardson et al. [29] by comparing the intensity ratios of the  $\text{Tb}^{3+}$  electronic transitions in two different aqueous solutions. There, they suggested that transitions with an *even*  $\Delta J$  are more sensitive to the ligand environment. Electronic transitions with this behavior are called hypersensitive and have been experimentally observed to follow the selection rule  $\Delta J = \pm 2$  in several aqueous solutions [30]. Judd [31] proposed that this effect is possible just for some symmetry groups:  $C_s$ ,  $C_1$ ,  $C_2$ ,  $C_3$ ,  $C_4$ ,  $C_6$ ,  $C_{2v}$ ,  $C_{3v}$ ,  $C_{4v}$  and  $C_{6v}$ , although some exceptions have been found [32]. Therefore, the  $^3\text{D}_4 \rightarrow ^7\text{F}_2$  transition could be considered hypersensitive and its intensity would strongly depend on the crystal field surrounding the  $\text{Tb}^{3+}$  ions.

## B. Density functional theory calculations

We used DFT calculations to determine the preferred Tb sites in the lattice. Simulations were carried out using the Vienna Ab initio Simulation Package (VASP) [33, 34]. To describe the exchange correlation density functional, we used the Perdew-Bruke-Enzerhof (PBE) generalized gradient approximation (GGA). All the calculations were performed with spin polarization, a cut-off energy of 400 eV, energy threshold of  $10^{-6}$  eV, and full relaxation of atomic positions with a force threshold of 0.01 eV/Å. A  $k$ -points grid of  $3 \times 3 \times 3$  following the Monkhorst Pack scheme was used to sample the Brillouin zone, and a smearing of 0.02 eV was applied.

The starting point of our calculations was the study of  $\text{In}_2\text{O}_3$  bixbyite structure carried by Marezio [35], from which the unit cell was obtained. The cubic bixbyite structure has two non-equivalent cationic positions corresponding to  $d$  and  $b$  sites in the Wickoff notation, each coordinated to six oxygen atoms. The  $d$  sites are low-symmetry positions where the cation is located at the center of a distorted cube with two oxygen vacancies along one of its face diagonals, corresponding to a  $C_2$  symmetry with the rotation axis aligned with the  $z$ -axis. In contrast, the  $b$  sites are higher-symmetry positions, where the cation sits at the center of a cube with two oxygen vacancies along one of its body diagonals, leading to a trigonally compressed octahedra [36]. The latter site corresponding to an  $S_6$  symmetry with the rotation axis parallel to  $z$ -axis, as illustrated in Figure 2.

When  $\text{In}_2\text{O}_3$  is doped with  $\text{SnO}_2$  to form ITO, the  $\text{Sn}^{4+}$  ion substitutes for the  $\text{In}^{3+}$  ions, preferentially occupying  $b$  sites. Then,  $\text{Sn}^{4+}$  contributes with an extra electron, increasing the carrier density while preserving the cubic structure. Tripathi et al. [37] studied the preferable positions of Sn impurities within the  $\text{In}_2\text{O}_3$  structure. They conclude that the  $b$  position is preferable when compared to  $d$  sites. Figure 3(a) shows the ITO unit cell with 6% of Sn in the  $b$  sites. The atomic coordinates of this system can be found in the supple-

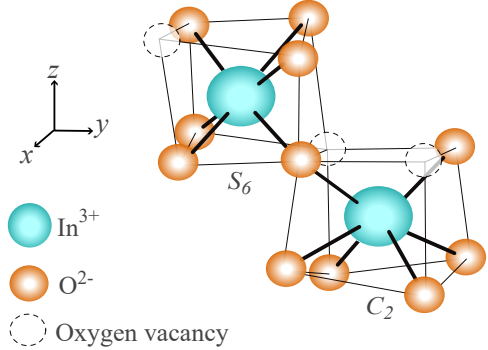


**FIG. 2:** Schematic presentation of the  $C_2$  and  $S_6$  symmetry sites in a cubic bixbyite. Used coordinate axis for the crystal field analysis are shown. The rotational axis is aligned along the  $z$ -direction.

mentary information.

When RE elements as Er, Nd, Eu or Tb are added, the ITO bixbyite structure remains stable as long as the solubility limit is not exceeded [22, 24]. Moreover, a theoretical analysis using first-principles methods, performed by Stanek et al. [38], showed that trivalent RE dopants in oxides with the bixbyite structure tend to localize at  $d$  sites when the solute cation is smaller than the host lattice cation, as this is energetically favorable. However, when the solute cation is larger than the host lattice cation, the  $b$  sites may also be preferred. In case of Tb-doped ITO, Tb ions can substitute either In or Sn ions in the  $b$  or  $d$  sites, inducing stress in the lattice due to the fact that the ionic radius of the six-coordinate  $\text{Tb}^{3+}$  ion ( $r=0.92$  Å) [39, 40] is larger than the radius of both  $\text{In}^{3+}$  ( $r=0.80$  Å) and  $\text{Sn}^{4+}$  ( $r=0.72$  Å) [41]. Indeed, the as-grown Tb-doped ITO layer exhibited an amorphous structure due to the active cooling of the sample holder during growth. After annealing at 550 °C, it crystallizes into the cubic bixbyite-type ( $Ia\bar{3}$ ) structure [25].

Here we performed the simulation of a unit cell with 80 atoms with  $8b$  sites and  $24d$  sites. The 3% of Tb incorporation was done by substituting In atoms only, keeping the 6% of Sn in ITO. This results in 30 possible positions for Tb. Nevertheless, many of these configurations have equivalent energy states. To differentiate them, we calculate the distance between Tb and both Sn atoms. This approach left 7 configurations with different in energies, three with Tb at  $b$  sites ( $\text{Tb}_{\text{In}2}$ ,  $\text{Tb}_{\text{In}4}$ , and  $\text{Tb}_{\text{In}6}$ ), and four with Tb at  $d$  sites ( $\text{Tb}_{\text{In}13}$ ,  $\text{Tb}_{\text{In}14}$ ,  $\text{Tb}_{\text{In}15}$ , and  $\text{Tb}_{\text{In}16}$ ). These can be seen in Figure 3(b) where the possible Tb positions are highlighted in yellow. The relative energies of the seven configurations can be found in Table II, where the lowest energy corresponds to the  $\text{Tb}_{\text{In}14}$  system. This indicate that Tb atoms prefer  $d$  sites over  $b$  sites. In addition, we have calculated the relative probability of a given state in thermodynamic equilibrium at certain temperature given by the Boltzmann factor,  $p_i$ , i.e.,

$$p_i = \exp(E_i/k_B T) \quad (2)$$

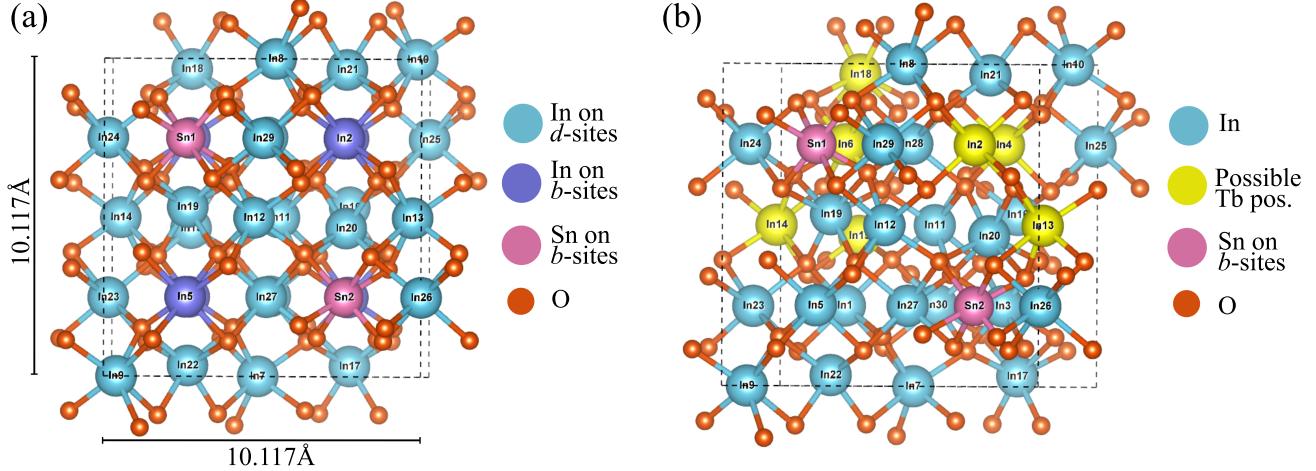


**FIG. 3:** ITO bixbyite structure with 6% of Sn located on *b* sites,  $\text{In}_{30}\text{Sn}_2\text{O}_{48}$ . Indium sites are marked with sky-blue and purple colors to point distinction of *b* and *d* sites (a). Possible positions of Tb within the ITO matrix are colored as yellow (b).

The relative probabilities for each configuration was calculated for 300K and 923K, representing room and annealing temperatures, respectively. The results show that at room temperature, the Tb atoms prefer *d* sites. Although at 923 K there is an enhancement of the probability for both sites, *d* sites are still the most probable ones.

**TABLE II:** Relative energies ( $E_i$ ) and Boltzmann probability factor ( $p_i$ ) calculated at 300K and 923K.

System	$E_i$ [meV]	$p_i$ at 300 K	$p_i$ at 923 K	Site	Symmetry
Tb <sub>In2</sub>	30	0.31	0.69	<i>b</i>	$S_6$
Tb <sub>In4</sub>	59	0.10	0.48	<i>b</i>	$S_6$
Tb <sub>In6</sub>	60	0.10	0.47	<i>b</i>	$S_6$
Tb <sub>In13</sub>	17	0.52	0.81	<i>d</i>	$C_2$
Tb <sub>In14</sub>	0	1.00	1.00	<i>d</i>	$C_2$
Tb <sub>In15</sub>	5	0.82	0.94	<i>d</i>	$C_2$
Tb <sub>In18</sub>	7	0.76	0.92	<i>d</i>	$C_2$

### C. Crystal field parametrization of the energy levels of $\text{Tb}^{3+}$ ions in $C_2$ symmetry sites

The complete Crystal Field (CF) energy levels scheme of the  $\text{Tb}^{3+}$  ion consists in a total of 3003 Stark levels [42]. However, here we have only considered the first 49 lowest  $^7F_{JM}$  set of levels. Since the CF operators only mix levels with the same multiplicity, in this case  $^7F_J$ . Furthermore, the substantial energy gap between the  $^5D_4$  excited state and the ground  $^7F_J$  levels makes  $J$ -mixing effects on the excited states negligible [42, 43], thus the latter approximation is valid.

The luminescence spectrum at 83 K under UV excitation was carefully fitted using the sum of 30 gaussian curves. The most energetic transition was observed

around  $20\,550\,\text{cm}^{-1}$  corresponding to the  $^5D_4 \rightarrow ^7F_6$  transition. Consistency criteria were imposed to improve the fitting accuracy. For each  $2J+1$  level, the full width at half maximum (FWHM) has to decrease as the transition energy increases [43, 44], as shown for the fitted parameters of the  $^5D_4 \rightarrow ^7F_2$  transition listed in Table III. Furthermore, this transition was resolved in a maximum of five peaks, as evidence in Figure 4, due to Stark splitting of the  $^7F_2$  multiplet, indicating that the  $\text{Tb}^{3+}$  ions are located at low-symmetry sites [45].

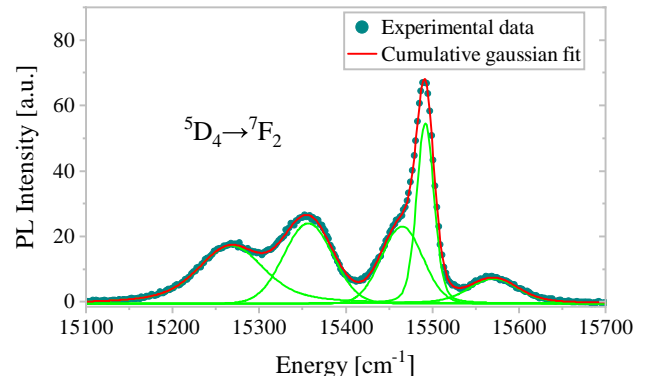


**FIG. 4:** High resolution spectrum of the  $^5D_4 \rightarrow ^7F_2$  transition at 83 K. The corresponding five peaks have been deconvoluted as explained in the text.

All energy levels were determined relative to the ground state at  $^7F_6$ , assuming that all visible transitions originate from a single  $^5D_4$  level at  $20\,550\,\text{cm}^{-1}$  ( $\sim 2.55\,\text{eV}$ ). This is confirmed by the PL measurements under 488nm ( $\sim 2.54\,\text{eV}$ ) excitation, which are quasi-resonant with the  $^5D_4 \rightarrow ^7F_6$  transition. In addition, the number of peaks in which the  $^5D_4 \rightarrow ^7F_2$  can be resolved suggest that the initial  $^5D_4$  state is not split.

**TABLE III:** Best fitted parameters of the Gaussian curves used to fit the  $^5D_4 \rightarrow ^7F_2$  transition at 83 K.

Transition	center [cm $^{-1}$ ]	FWHM [cm $^{-1}$ ]	Integrate intensity [a.u.]
$^5D_4 \rightarrow ^7F_2$	15260	83	146374
	15355	74	200934
	15469	54	163258
	15494	23	121184
	15570	66	52505

The experimental energy levels of  $Tb^{3+}$  were fitted using a parametric Hamiltonian for the  $4f^8$  configuration, which can be written as a free-ion (fi) part and crystal field (CF) parts [46]:

$$H = H_{\text{fi}} + H_{\text{CF}} \quad (3)$$

Here the free-ion Hamiltonian  $H_{\text{fi}}$  includes all spherically symmetric interactions, and is expressed as:

$$\begin{aligned} H_{\text{fi}} = & E_{\text{avg}} + \sum_{k=2,4,6} F^k \mathbf{f}_k + \zeta_{4f} \mathbf{A}_{\text{SO}} \\ & + \alpha L(L+1) + \beta G(G_2) + \gamma G(R_7) \\ & + \sum_{i=2,3,4,6,7,8} T^i t_i + \sum_{k=0,2,4} M^k m_k + \sum_{k=2,4,6} P^k p_k. \end{aligned} \quad (4)$$

Here the first term,  $E_{\text{avg}}$ , represents the barycenter energy of the  $f^8$  configuration. The second term describes the Coulomb interactions between the  $4f^8$  electrons, splitting the  $f^8$  configuration into  $SL$  terms.  $F^k$  are the Slater parameters, and  $\mathbf{f}_k$  represents the angular part of the electrostatic interaction operator. The third term accounts for spin-orbit (SO) coupling, involving the SO constant  $\zeta_{4f}$  and the angular part  $\mathbf{A}_{\text{SO}}$  of the interaction operator. The last six terms involve up to 15 correction and correlations factors. Where  $\alpha, \beta, \gamma$  are the two-particle configuration interaction parameters. Here  $L$  is the total orbital angular momentum,  $G(G_2)$  and  $G(R_7)$  are Casimir operators for groups  $G_2$  and  $R_7$ . The  $T^i$  parameters are associated with the three-particle operators  $t_i$ .  $M^k$  correspond to Marvin integrals with  $m_k$  as their associated operators.  $P^k$  are electrostatic correlated SO interaction parameters with  $p_k$  being the associated operators. Although these latter terms provide only minor corrections and do not induce energy level splitting, omitting them would compromise the accuracy of the fit. Further details are available in [46–49].

Following Wybourne formalism, the crystal field Hamiltonian  $H_{\text{CF}}$  can be written as [50]:

$$H_{\text{CF}} = \sum_k \sum_{q=-k}^k \left[ B_q^k [C_q^k + (-1)^q C_{-q}^k] + i S_q^k [C_q^k + (-1)^q C_{-q}^k] \right]. \quad (5)$$

where  $C_q^k$  are the spherical tensor operators for the  $4f^n$  configuration. The  $B_q^k$  and  $S_q^k$  are the real and imaginary

parts of the CF parameters with  $k = 0, 2, 4, 6$  and  $q \neq 0$ . The CF parameters fitting was performed using the  $f$ -shell empirical programs provided by M. F. Reid [51].

Based on the observed  $^5D_4 \rightarrow ^7F_2$  and DFT calculations, we assume that the emission of the Tb-doped ITO layer is due to  $Tb^{3+}$  ions mainly located at  $C_2$  symmetry sites of the ITO bixbyite structure.  $H_{\text{CF}}$  is expanded in terms of the  $C_2$  symmetry as [50, 52]:

$$\begin{aligned} H_{\text{CF}} = & B_0^2 C_0^2 + B_2^2 (C_{-2}^2 + C_2^2) + i S_2^2 (C_{-2}^2 + C_2^2) + B_0^4 C_0^2 \\ & + B_2^4 (C_{-2}^4 + C_2^4) + i S_2^4 (C_{-2}^4 + C_2^4) + B_4^4 (C_{-4}^4 + C_4^4) \\ & + i S_4^4 (C_{-4}^4 + C_4^4) + B_0^6 C_0^6 + B_2^6 (C_{-2}^6 + C_2^6) \\ & + i S_2^6 (C_{-2}^6 + C_2^6) + B_4^6 (C_{-4}^6 + C_4^6) + i S_4^6 (C_{-4}^6 + C_4^6) \\ & + B_6^6 (C_{-6}^6 + C_6^6) + i S_6^6 (C_{-6}^6 + C_6^6) \end{aligned} \quad (6)$$

The total number of CF parameters is 15, considering the real and imaginary parts. However, by choosing an appropriate axis rotation, the parameter  $S_2^2$  can be fixed to zero, the  $z$ -axis is the most common choice [43, 52, 53].

The starting values for the free-ion parameters were taken from Carnall et al. [46] for  $\text{LaF}_3:\text{Tb}^{3+}$ ,  $F^2 = 88\,995 \text{ cm}^{-1}$ ,  $F^4 = 62\,919 \text{ cm}^{-1}$ ,  $F^6 = 47\,252 \text{ cm}^{-1}$ , and  $\zeta_{4f} = 1707 \text{ cm}^{-1}$ , as well as the correction and correlation factors  $\alpha, \beta, \gamma, T^i, M^h, P^k$ . The latter were kept fixed throughout the entire fitting procedure since this

**TABLE IV:** Crystal field energies (in  $\text{cm}^{-1}$ ) of the  $Tb^{3+}$  ion in the indium tin oxide (ITO) determined based on the emission spectra from the  $^5D_4$  multiplets taken at 87 K. For  $f - f$  transitions in sites of  $C_2$  local symmetry  $2J + 1$  lines are expected.

SLJ Level	Exp	Fit	SLJ Level	Exp	Fit
$^7F_6$	0	-6.6	$^7F_3$	3398	3402
	-	18.6		3522	3528
	-	42.3		3584	3585
	107	109		-	3604
	-	110		-	3686
	147	148		3783	3725
	-	150		3852	3850
	362	371		3906	3899
	-	374		4023	4028
	-	511		4080	4076
	-	512		4331	4329
	-	646		4347	4333
	659	655		4532	4534
	-	717		-	4629
	2138	2154		4667	4660
	2194	2162	$^7F_2$	4906	4910
	2302	2311		5053	5039
	2373	2384		5078	5072
	-	2509		5202	5222
	-	2644		5287	5284
$^7F_5$	2795	2794	$^7F_1$	-	5424
	2875	2868		-	5457
	3026	3027		-	5650
	-	3142		$^7F_0$	-
	3327	3332		-	5656

**TABLE V:** Free Ion and crystal field parameters (in  $\text{cm}^{-1}$ ) for  $\text{Tb}^{3+}$  in the  $C_2$  site of  $Ia\bar{3}$  ITO thin film at 83 K.  $\sigma$  is the root mean square (rms) deviation between calculated and observed energies. The uncertainty associated with each parameter is indicated in parenthesis. Parameters in brackets were kept fixed during the fitting. ( $M^2 = 0.56M^0$ ,  $M^4 = 0.31M^0$ ,  $P^4 = 0.5P^2$ , and  $P^6 = 0.1P^2$ ).

Parameter	Value	Parameter	Value
$E_{\text{avg}}$	67044 (196)	$B_0^2$	-750 (90)
$F^2$	95528 (503)	$B_2^2$	-1006 (63)
$F^4$	44544 (889)	$B_0^4$	-2275 (196)
$F^6$	52352 (555)	$B_2^4$	-2226 (150)
$\zeta_{4f}$	902 (19)	$S_2^4$	2298 (114)
$T^2$	[320]	$B_4^4$	2163 (225)
$T^3$	[40]	$S_4^4$	1849 (212)
$T^4$	[50]	$B_0^6$	-781 (152)
$T^6$	[395]	$B_2^6$	1899 (214)
$T^7$	[303]	$S_2^6$	-4564 (152)
$T^8$	[317]	$B_4^6$	508 (226)
$\alpha$	[18.4]	$S_4^6$	-2486 (112)
$\beta$	[-591]	$B_6^6$	-2834 (114)
$\gamma$	[1650]	$S_6^6$	276 (411)
$M^0$	[2.39]		
$P^2$	[373]	$\sigma$	15.1

parameters only change approximately 1% for different lattices [1]. The initial values of the CF parameters were taken from Leavitt et al. [54]:  $B_0^2 = -186 \text{ cm}^{-1}$ ,  $B_2^2 = -695 \text{ cm}^{-1}$ ,  $B_0^4 = -1329 \text{ cm}^{-1}$ ,  $B_2^4 = -1286 \text{ cm}^{-1}$ ,  $S_2^4 = 192 \text{ cm}^{-1}$ ,  $B_4^4 = 727 \text{ cm}^{-1}$ ,  $S_4^4 = -921 \text{ cm}^{-1}$ ,  $B_0^6 = 258 \text{ cm}^{-1}$ ,  $B_2^6 = 306 \text{ cm}^{-1}$ ,  $S_2^6 = 68 \text{ cm}^{-1}$ ,  $B_4^6 = 459 \text{ cm}^{-1}$ ,  $S_4^6 = -348 \text{ cm}^{-1}$ ,  $B_6^6 = -33 \text{ cm}^{-1}$ , and  $S_6^6 = -35 \text{ cm}^{-1}$ . These values correspond to the CF parameters of  $\text{Tb}^{3+}$  at  $C_2$  symmetry sites of  $\text{Y}_2\text{O}_3$ , with a root mean square deviation (rms) of  $\sigma = 7.0 \text{ cm}^{-1}$ . Initially, the free-ion parameters were kept fixed while the CF parameters were allowed to vary. In the subsequent iteration, the fitting process was performed using the calculated CF parameters as starting values, and allowing the free-ion parameters to vary. The experimental and the calculated energy levels are listed in Table IV, and the optimized set of the fitted free-ion and CF parameters are given in Table V. CF calculations show good overall agreement between the calculated and experimental CF energy levels, resulting in an rms deviation of  $\sigma = 15.1 \text{ cm}^{-1}$ .

The obtained CF parameters are similar to those found for  $\text{Tb}^{3+}$  in  $\text{Y}_2\text{O}_3$  [54],  $\text{Eu}^{3+}$  in  $\text{Eu}_2\text{O}_3$  [43], and  $\text{Eu}^{3+}$  in  $\text{In}_2\text{O}_3$  [53] ( $\text{Eu}^{3+}$  has also 49 CF energy levels related to the  $7F_J$  multiplet). In all these crystals the rare earth

ion is in  $C_2$  symmetry sites in a bixbyite structure. The parameters are also similar to those for  $\text{Tb}^{3+}$  at  $C_2$  symmetry sites in ortho-aluminate  $\text{TbAlO}_3$  with a perovskite structure [55, 56].

#### IV. SUMMARY

In this work we have analyzed the local symmetry of the trivalent terbium ions embedded in indium tin oxide matrix with bixbyite structure. In this matrix,  $\text{Tb}^{3+}$  could in principle substitute  $\text{In}^{3+}$  ions in two different cationic positions,  $d$  or  $b$  sites, inducing stress in the lattice. DFT calculations showed that Tb atoms prefer the  $C_2$  symmetry at  $d$  sites over  $S_6$  symmetry at  $b$  sites, thus it is highly likely that  $\text{Tb}^{3+}$  takes a low symmetry site in the bixbyite structure i.e.  $C_2$  symmetry sites. This symmetry relaxes selection rules allowing electric dipole transitions that are forbidden in the free rare earth ion. It was found that the  $^5D_4 \rightarrow ^7F_2$  transition exhibits the highest intensity in photoluminescence spectra of the  $\text{Tb}^{3+}$ , providing a unusual red color to the Tb-related light emission spectrum, and can be resolve in five peaks as a result of Stark splitting induced by inhomogeneities in the crystal field surrounding. A total of 30 intra-4f transitions were identified from the Tb-doped ITO photoluminescence emission spectrum under UV excitation (325 nm) at 83 K. The energy levels corresponding to the  $7F_J$  ground multiplet were used to compute the crystal field parameters yielding a final standard deviation of  $\sigma = 15.1 \text{ cm}^{-1}$ . The values of the crystal field parameters are similar to those found for  $\text{Tb}^{3+}$  at  $C_2$  sites in other hosts materials. Thus confirming that light emitting  $\text{Tb}^{3+}$  ions occupy mainly  $C_2$  symmetry sites in the ITO bixbyite structure. These results highlight the capability of tuning the color emission of the  $\text{Tb}^{3+}$  ions by controlling their atomic environment.

#### V. ACKNOWLEDGMENTS

This work was funded by the Office of Naval Research (ONR), Grant No. N62909-21-1-2034. E. Serquen acknowledges the Peruvian National Council for Science, Technology and Technological Innovation (CONCYTEC) and the Peruvian National Program of Scientific Research and Advanced Studies (PROCIENCIA), funding scheme E073-2023-01, Grant No. PE501085403-2023. K. Lizárraga and P. Venezuela acknowledge thank the CNPq for the grant 153707/2024-0 under the project 406447/2022-5 Materials Informatics. L. R. Tessler and J. A. Guerra recognize to the DARI-PUCP support for travel expenses. The authors are indebted to the Center for Characterization of Materials (CAM-PUCP) facilities where the experimental characterization was conducted.

[1] G. Liu, *Spectroscopic Properties of Rare Earths in Optical Materials*, edited by R. Hull, J. Parisi, R. M. Osgood,

H. Warlimont, G. Liu, and B. Jacquier (Springer Berlin Heidelberg, Berlin, Heidelberg, 2005) pp. 1–94.

- [2] B. M. Walsh, Judd-Ofelt theory: principles and practices, in *Advances in Spectroscopy for Lasers and Sensing*, edited by B. Di Bartolo and O. Forte (Springer Netherlands, Dordrecht, 2006) pp. 403–433.
- [3] J. A. Guerra, F. Benz, A. R. Zanatta, H. P. Strunk, A. Winnacker, and R. Weingärtner, Concentration quenching and thermal activation of the luminescence from terbium-doped a-SiC:H and c-AlN thin films, *physica status solidi c* **10**, 68 (2013).
- [4] Q. Wang, J. Li, W. Zhang, H. Zheng, and R. Cong, Synthesis, and photoluminescence and magnetic properties of Tb-doped AlN single-crystalline nanobelts, *Journal of Luminescence* **236**, 118089 (2021).
- [5] J. A. Guerra, F. D. Zela, K. Tucto, L. Montañez, J. A. Töfflinger, A. Winnacker, and R. Weingärtner, Effect of thermal annealing treatments on the optical activation of Tb<sup>3+</sup>-doped amorphous SiC:H thin films, *Journal of Physics D: Applied Physics* **49**, 375104 (2016).
- [6] Q. Guo, Y. Koga, Z. Chen, K. Saito, and T. Tanaka, Growth and characteristics of terbium doped Ga<sub>2</sub>O<sub>3</sub> luminescent films, *Journal of Crystal Growth* **620**, 127361 (2023).
- [7] G. B. F. Bosco, Z. Khatami, J. Wojcik, P. Mascher, and L. R. Tessler, Excitation Mechanism of Tb<sup>3+</sup> in a-Si<sub>3</sub>N<sub>4</sub>:H under Sub-Gap Excitation, *Journal of Luminescence* **202**, 327–331 (2018).
- [8] C. Braun, L. Mereacre, Z. Chen, and A. Slabon, Closing the yellow gap with Eu-and Tb-doped GaN: one luminescent host resulting in three colours, *Scientific Reports* **12**, 2503 (2022).
- [9] S. Devi, A. Khatkar, V. Taxak, A. Hooda, P. Sehrawat, S. Singh, and S. Khatkar, Influence of Tb<sup>3+</sup> doping on the structural and down-conversion luminescence behaviour of SrLaAlO<sub>4</sub> nanophosphor, *Journal of Luminescence* **221**, 117064 (2020).
- [10] R. M. J. Petoral, F. Söderlind, A. Klasson, A. Suska, M. A. Fortin, N. Abrikossova, L. Selegård, P.-O. Käll, M. Engström, and K. Uvdal, Synthesis and characterization of tb<sup>3+</sup>-doped gd<sub>2</sub>O<sub>3</sub> nanocrystals: A bifunctional material with combined fluorescent labeling and mri contrast agent properties, *The Journal of Physical Chemistry C* **113**, 6913 (2009).
- [11] Y. Tahiri Alaoui and N. Semlali Aouragh Hassani, Leaching process for terbium recovery from linear tube fluorescent lamps: optimization by response surface methodology, *Environmental Science and Pollution Research* **27**, 45527 (2020).
- [12] Q. Zhu, S. Li, Q. Wang, Y. Qi, X. Li, X. Sun, and J.-G. Li, Grafting of terbium(iii) complexes onto layered rare-earth hydroxide nanosheets to fabricate novel optical fiber temperature sensors, *Nanoscale* **11**, 2795 (2019).
- [13] Q. Guo, Y. Koga, Z. Chen, K. Saito, and T. Tanaka, Characteristics of Light-Emitting Diodes Based on Terbium-Doped Ga<sub>2</sub>O<sub>3</sub> Films, *physica status solidi (RRL) – Rapid Research Letters* **18**, 2300481 (2024).
- [14] D. De Graaf, S. Stelwagen, H. Hintzen, and G. De With, Tb<sup>3+</sup> luminescence as a tool to study clustering of lanthanide ions in oxynitride glasses, *Journal of non-crystalline solids* **325**, 29 (2003).
- [15] J. dos Santos, V. Zanuto, A. Soares, E. Savi, L. Nunes, M. Baesso, and T. Catunda, Evaluating the link between blue-green luminescence and cross-relaxation processes in Tb<sup>3+</sup>-doped glasses, *Journal of Luminescence* **240**, 118430 (2021).
- [16] F. Benz, H. P. Strunk, J. Schaab, U. Künecke, and P. Wellmann, Tuning the emission colour by manipulating terbium-terbium interactions: Terbium doped aluminum nitride as an example system, *Journal of Applied Physics* **114**, 073518 (2013).
- [17] Z. Ma, Z. Li, K. Liu, C. Ye, and V. J. Sorger, Indium-Tin-Oxide for High-performance Electro-optic Modulation, *Nanophotonics* **4**, 198 (2015).
- [18] A. S. Pereira, M. Peres, M. J. Soares, E. Alves, A. Neves, T. Monteiro, and T. Trindade, Synthesis, surface modification and optical properties of tb<sup>3+</sup>-doped zno nanocrystals, *Nanotechnology* **17**, 834 (2006).
- [19] P. Sakthivel, S. Asaithambi, M. Karuppaiah, S. Sheikfared, R. Yuvakkumar, and G. Ravi, Different rare earth (sm, la, nd) doped magnetron sputtered cdo thin films for optoelectronic applications, *Journal of Materials Science: Materials in Electronics* **30**, 9999 (2019).
- [20] H. Çolak and E. Karaköse, Tm-doped zno nanorods as a tco for pv applications, *Journal of Rare Earths* **36**, 1067 (2018).
- [21] J. Gil-Rostra, F. Yubero Valencia, and A. R. González-Elipe, Thin film electroluminescent device based on magnetron sputtered tb doped zngao<sub>2</sub>O<sub>4</sub> layers, *Journal of Luminescence* **228**, 117617 (2020).
- [22] Y. G. Choi, S. M. Yu, and W. J. Chung, Local structural environment and photoluminescence of Er<sup>3+</sup> ions doped in indium tin oxide nanopowder, *Chemical Physics Letters* **461**, 290 (2008).
- [23] J. K. Kim and Y. G. Choi, Eu-doped indium tin oxide thin films fabricated by sol-gel technique, *Thin Solid Films* **517**, 5084 (2009).
- [24] T. O. L. Sunde, M. Lindgren, T. O. Mason, M.-A. Einarsrud, and T. Grande, Solid solubility of rare earth elements (Nd, Eu, Tb) in In<sub>2-x</sub>Sn<sub>x</sub>O<sub>3</sub> – effect on electrical conductivity and optical properties, *Dalton Trans.* **43**, 9620 (2014).
- [25] P. Llontop, C. E. Torres, M. Piñeiro, L. Conde, A. Tejada, J. A. Töfflinger, F. Rumiche, F. F. H. Aragón, D. G. Pacheco-Salazar, R. Grieseler, L. Korte, and J. A. Guerra, Indirect excitation and luminescence activation of Tb doped indium tin oxide and its impact on the host's optical and electrical properties, *Journal of Physics D: Applied Physics* **55**, 210002 (2022).
- [26] Y.-C. Li, Y.-H. Chang, Y.-S. Chang, Y.-J. Lin, and C.-H. Laing, Luminescence and energy transfer properties of gd<sup>3+</sup> and tb<sup>3+</sup> in laalge<sub>2</sub>O<sub>7</sub>, *The Journal of Physical Chemistry C* **111**, 10682 (2007).
- [27] K. Irmscher, M. Naumann, M. Pietsch, Z. Galazka, R. Uecker, T. Schulz, R. Schewski, M. Albrecht, and R. Fornari, On the nature and temperature dependence of the fundamental band gap of In<sub>2</sub>O<sub>3</sub>, *physica status solidi (a)* **211**, 54 (2014).
- [28] C. Görller-Walrand and K. Binnemans, Chapter 167 spectral intensities of f-f transitions (Elsevier, 1998) pp. 101–264.
- [29] S. A. D. Frederick S. Richardson, Jeffrey D. Saxe and T. R. Faulkner, Intensity calculations on hypersensitive f-f transitions in nine-coordinate lanthanide systems of trigonal symmetry, *Molecular Physics* **42**, 1401 (1981).
- [30] C. K. Jørgensen and B. Judd, Hypersensitive pseudo-quadrupole transitions in lanthanides, *Molecular Physics* **8**, 281 (1964).
- [31] B. R. Judd, Hypersensitive transitions in rare-earth ions, *The Journal of Chemical Physics* **44**, 839 (1966).

- [32] K. Binnemans, Interpretation of europium(iii) spectra, *Coordination Chemistry Reviews* **295**, 1 (2015).
- [33] G. Kresse and J. Furthmüller, Efficient iterative schemes for ab initio total-energy calculations using a plane-wave basis set, *Phys. Rev. B* **54**, 11169–11186 (1996).
- [34] G. Kresse and J. Hafner, Ab initio molecular dynamics for liquid metals, *Phys. Rev. B* **47**, 558 (1993).
- [35] M. Marezio, Refinement of the crystal structure of  $\text{In}_2\text{O}_3$  at two wavelengths, *Acta Crystallographica* **20**, 723 (1966).
- [36] N. Nadaud, N. Lequeux, M. Nanot, J. Jové, and T. Roisnel, Structural Studies of Tin-Doped Indium Oxide (ITO) and  $\text{In}_4\text{Sn}_3\text{O}_{12}$ , *Journal of Solid State Chemistry* **135**, 140 (1998).
- [37] M. N. Tripathi *et al.*, First-principles analysis of structural and opto-electronic properties of indium tin oxide, *Journal of Applied Physics* **111**, 103110 (2012).
- [38] C. R. Stanek, K. J. McClellan, B. P. Uberuaga, K. E. Sickafus, M. R. Levy, and R. W. Grimes, Determining the site preference of trivalent dopants in bixbyite sesquioxides by atomic-scale simulations, *Phys. Rev. B* **75**, 134101 (2007).
- [39] D. H. Templeton and C. H. Dauben, Lattice parameters of some rare earth compounds and a set of crystal radii, *Journal of the American Chemical Society* **76**, 5237 (1954).
- [40] S. K. Gupta, P. S. Ghosh, A. K. Yadav, N. Pathak, A. Arya, S. N. Jha, D. Bhattacharyya, and R. M. Kadam, Luminescence Properties of  $\text{SrZrO}_3/\text{Tb}^{3+}$  Perovskite: Host-Dopant Energy-Transfer Dynamics and Local Structure of  $\text{Tb}^{3+}$ , *Inorganic Chemistry* **55**, 1728 (2016).
- [41] F.-J. Meng and X.-M. Guo, Tuning the oxygen defects and Fermi levels via  $\text{In}^{3+}$  doping in  $\text{SnO}_2\text{-In}_2\text{O}_3$  nanocomposite for efficient CO detection, *Sensors and Actuators B: Chemical* **357**, 131412 (2022).
- [42] E. Antic-Fidancev, J. Hölsä, J.-C. Krupa, and M. Lastusaari, Crystal fields in ROF:Tb $^{3+}$  (R = La, Gd), *Journal of Alloys and Compounds* **380**, 303 (2004).
- [43] G. B. Bosco and L. R. Tessler, Crystal field parameters of the  $\text{C}_2$  site in  $\text{Eu}_2\text{O}_3$ , *Optical Materials: X* **2**, 100028 (2019).
- [44] S. Taboada, A. de Andrés, J. E. Muñoz Santustre, C. Prieto, J. L. Martínez, and A. Criado, Optical phonons, crystal-field transitions, and europium luminescence excitation processes in  $\text{Eu}_2\text{BaCoO}_5$ : Experiment and theory, *Phys. Rev. B* **50**, 9157 (1994).
- [45] A. de Bettencourt-Dias, Lanthanides: Electronic Structure, in *Encyclopedia of Inorganic and Bioinorganic Chemistry* (John Wiley & Sons, Ltd, 2012).
- [46] W. T. Carnall, G. L. Goodman, K. Rajnak, and R. S. Rana, A systematic analysis of the spectra of the lanthanides doped into single crystal  $\text{LaF}_3$ , *The Journal of Chemical Physics* **90**, 3443 (1989).
- [47] M. F. Reid, Theory of Rare-Earth Electronic Structure and Spectroscopy, *Handbook on the Physics and Chemistry of Rare Earths* **50**, 47 (2016).
- [48] M. G. Brik and M. Chong-Geng, *Theoretical spectroscopy of transition metal and rare earth ions: from free state to crystal field* (CRC Press, 2019).
- [49] D. J. Newman and B. Ng, *Crystal field handbook*, Vol. 43 (Cambridge University Press, 2000).
- [50] B. G. Wybourne and W. F. Meggers, Spectroscopic properties of rare earths (1965).
- [51] M. Reid, *f*-shell Empirical Programs, University of Canterbury, New Zealand (1984).
- [52] M. Karbowiak, P. Gnutek, and C. Rudowicz, Reanalysis of energy levels and crystal field parameters for  $\text{Er}^{3+}$  and  $\text{Tm}^{3+}$  ions at  $\text{C}_2$  symmetry sites in hexahydrated trichloride crystals—Intricate aspects of multiple solutions for monoclinic symmetry, *Physica B: Condensed Matter* **405**, 1927 (2010).
- [53] E. Antic-Fidancev, J. Hölsä, and M. Lastusaari, Crystal field strength in C-type cubic rare earth oxides, *Journal of Alloys and Compounds* **341**, 82 (2002).
- [54] R. P. Leavitt, J. B. Gruber, N. C. Chang, and C. A. Morrison, Optical spectra, energy levels, and crystal-field analysis of tripositive rare-earth ions in  $\text{Y}_2\text{O}_3$ . II. Non-Kramers ions in  $\text{C}_2$  sites, *The Journal of Chemical Physics* **76**, 4775 (1982).
- [55] C. Rudowicz, P. Gnutek, and M. Brik, Low symmetry aspects in spectroscopic and magnetic susceptibility studies of  $\text{Tb}^{3+}(4f^8)$  in  $\text{TbAlO}_3$ , *Journal of Rare Earths* **27**, 627 (2009).
- [56] J. B. Gruber, K. L. Nash, R. M. Yow, D. K. Sardar, U. V. Valiev, A. A. Uzakov, and G. W. Burdick, Spectroscopic and magnetic susceptibility analyses of the  ${}^7\text{F}_J$  and  ${}^5\text{D}_4$  energy levels of  $\text{Tb}^{3+}(4f^8)$  in  $\text{TbAlO}_3$ , *Journal of Luminescence* **128**, 1271 (2008).